Efficient Pipeline for Image-Based Patient-Specific Analysis of Cerebral Aneurysm Hemodynamics: Technique and Sensitivity

Juan R. Cebral*, Marcelo A. Castro, Sunil Appanaboyina, Christopher M. Putman, Daniel Millan, and Alejandro F. Frangi, *Member, IEEE*

***Abstract*—Hemodynamic factors are thought to be implicated in the progression and rupture of intracranial aneurysms. Current efforts aim to study the possible associations of hemodynamic characteristics such as complexity and stability of intra-aneurysmal flow patterns, size and location of the region of flow impingement with the clinical history of aneurysmal rupture. However, there are no reliable methods for measuring blood flow patterns *in vivo*. In this paper, an efficient methodology for patient-specific modeling and characterization of the hemodynamics in cerebral aneurysms from medical images is described. A sensitivity analysis of the hemodynamic characteristics with respect to variations of several variables over the expected physiologic range of conditions is also presented. This sensitivity analysis shows that although changes in the velocity fields can be observed, the characterization of the intra-aneurysmal flow patterns is not altered when the mean input flow, the flow division, the viscosity model, or mesh resolution are changed. It was also found that the variable that has the greater impact on the computed flow fields is the geometry of the vascular structures. We conclude that with the proposed modeling pipeline clinical studies involving large numbers cerebral aneurysms are feasible.**

***Index Terms*—Cerebral aneurysm, computational fluid dynamics, rotational angiography, sensitivity.**

I. Introduction

INTRACRANIAL aneurysms are pathological dilatations of cerebral arteries. They tend to occur at or near arterial bifurcations, mostly in the circle of Willis [40]. They can be roughly classified into terminal, lateral or bifurcation aneurysms depending on their relation to the parent vessel. The most serious complication happens when the aneurysm breaks. The risk of rupture varies with type, size, location, and history of previous aneurysm ruptures. Aneurysm rupture and subsequent subarachnoid hemorrhage has an incidence of sudden death of 12.4% and rates of fatality from 32% to 67% after the hemorrhage [9], [19]. Morbidity rates reach the 10.9% after surgical clipping, due to intracranial bruise, subsequent rebleeding, stroke, hydrocephaly, and spasms in the surrounding brain vessels [20], [23], [37], [44], [45]. Greater availability and improvement of neuroradiological techniques have resulted in more frequent detection of unruptured aneurysms. Because prognosis of subarachnoid hemorrhage is still poor, preventive surgery is increasingly considered as a therapeutic option. Planning elective surgery requires a better understanding of the process of aneurysm formation, progression, and rupture so that a sound judgment between the risks and benefits can be made. The reasons for genesis, growth and rupture of saccular aneurysms are not clear. However, hemodynamic factors, such as wall shear stress, pressure, residence time and flow impingement, are thought to play a role in the pathogenesis of aneurysms and thrombosis [21] and, therefore, may be important in therapeutic decision making [38].

Characterizing and measuring hemodynamic quantities pose a difficult challenge. Because measuring hemodynamic quantities *in vivo* is difficult and involve significant patient risk, various modeling approaches have been considered in the past [24]. Each of these approaches has had significant limitations in connecting the hemodynamic factors studied to a clinical event. *In vitro* studies have allowed very detailed measurement of hemodynamic variables in often idealized geometries, but cannot be used in a straight manner for understanding the hemodynamic forces in an individual clinical case. The creation of the patient specific geometrical models to be used in the investigation is currently impractical for large population studies. Without these studies, the correlation between patient specific clinical events and hemodynamic patterns cannot be assessed. Computational based models provide an attractive method of circumventing this problem by providing the ability to theoretically model and study all possible geometries. However, until recently computational studies have been only performed on idealized aneurysm geometries or approximations of a specific patient geometry. The obstacles for applying computational methods to large numbers of patient-specific aneurysm geometries are threefold. The first obstacle is obtaining the patient-specific geometry. The second is converting the geometry into a workable numerical model. The third obstacle is the computational power required to do the large numbers of calculations in a timely manner.

Manuscript received November 24, 2004; revised January 11, 2005. This work was supported in part by a grant from Fundación MAPFRE Medicina and grants TIC2002-04495-C02 from the MEyC, and FIS-PI040676 and G03/185 from ISCIII. The work of J. R. Cebral supported in part by The Whitaker Foundation and in part by Philips Medical Systems. The work of A. F. Frangi was supported in part by a Ramon y Cajal Research Fellowship from the Spanish MEyC. *Asterisk indicates corresponding author.*

*J. R. Cebral is with the School of Computational Sciences, George Mason University, 4400 University Drive, MSN 4C7, Fairfax, VA 22030 USA (e-mail: jcebral@gmu.edu).

M. A. Castro and S. Appanaboyina are with the School of Computational Sciences, George Mason University, Fairfax, VA 22030 USA.

C. M. Putman is with the Interventional Neuroradiology, Inova Fairfax Hospital, Fairfax, VA 22030 USA.

D. Millan and A. F. Frangi are with the Department of Technology, Pompeu Fabra University, Barcelona, Spain.

Digital Object Identifier 10.1109/TMI.2005.844159

Current advances in imaging now make 3-D data of human anatomy commonplace in the modern clinical practice. Techniques for reconstructing 3-D representations from computed tomography, magnetic resonance imaging, and ultrasonography are readily available. RA can provide high resolution images of the intracranial vascular anatomy as part of the routine evaluation of a patient with a cerebral aneurysm. These renderings have the potential to provide the basis for applying computational fluid dynamic (CFD) techniques to patient specific geometries. Recently, image-based CFD models have been constructed from medical images with very promising results [6], [7], [13]–[15], [22], [41] paving the way to using these techniques for diagnosis, therapeutic planning and follow up. To overcome the obstacle of laborious and lengthy data processing and calculations, the whole pipeline from medical images to flow simulations must be fully optimized with the goal of reducing or eliminating manual intervention and editing. Also, efficient image analysis and mesh generation techniques must be created to make the computational cost of the required CFD simulations practical for large-scale clinical studies. Additionally, mesh generation has to be capable of handling the realistic complex geometries of aneurysms and its connected vessels so that biases can be reduced in the studied populations for statistical analysis.

This paper presents a complete and efficient image-based methodology for the hemodynamic analysis of cerebral aneurysms on a patient-specific basis. Although the individual components of the modeling pipeline may not be entirely original, this methodology allows for the first time the modeling of a large number of aneurysms in a timely manner. In addition, preliminary aneurysm flow characterization variables are proposed and a sensitivity analysis is performed in order to study the dependence of intra-aneurysmal flow characteristics with respect to several model assumptions and input functions.

II. Methods

The pipeline for simulation-based analysis of cerebral aneurysm hemodynamics consists in the following stages:

1) vessel reconstruction from anatomical images;
2) unstructured grid generation;
3) numerical solution of the fluid flow equations;
4) postprocessing and visualization of the numerical results.

Using this pipeline, to date approximately 60 models have been created and classified into different categories according to different features of the aneurysmal hemodynamics [16]. The sensitivity of this classification with respect to several assumptions and model parameters is analyzed in a subset of four aneurysms. Namely, the sensitivity of the characterization with respect to the following variables was considered:

- mean input flow or total flow;
- flow division among arterial branches;
- accounting for small vessel branches;
- non-Newtonian viscosity;
- reconstruction process.

In the remainder of this section, a more detailed description of each stage of the simulation pipeline and of the sensitivity analysis are provided.

A. Modeling Vessels

Vessel Reconstruction: Personalized models of blood vessels are constructed from three-dimensional (3-D) rotational angiography (3DRA) images [13]–[16].

Two alternative approaches have been used, one based on deformable models and another based on the level set method. Briefly, the deformable model reconstruction proceeds as follows: the images are first smoothed using a combination of blurring and sharpening operations followed by a region growing segmentation and iso-surface extraction [14]. This surface is then used to initialize a deformable model under the action of internal smoothing forces and external forces from the gradients of the original un-processed images [32].

The second approach consists in a two-stage segmentation algorithm. In the first stage, a fast and rough segmentation is obtained by means of the fast marching method [39]. The speed used for the evolution of the boundary surface is based on a vessel enhancement filter [5]. The output of the fast marching algorithm yields an image of a function called action map. This function presents an abrupt jump of the time values in a neighborhood of the edges of the aneurysm and its surrounding vessels. This allows us to extract a presegmentation of the aneurysm using simply a threshold of the action map. In the second stage, this presegmentation is used as initialization for the geodesic active region model as follows. The presegmentation defines a partition of the image domain into regions corresponding to vessel and background. The histogram of the grey values for each of these regions is modeled by a Gaussian distribution. A propagation speed based on these descriptors is used in the equation of the surface evolution. The level set algorithm is used to track the motion of the embedding function. The final segmentation is the zero level set of the embedding function. The method has recently been introduced and extensively validated [8].

The reconstructed model is then smoothed using a nonshrinking algorithm [43], the triangulation is optimized using edge collapses and diagonal swaps [2], the vessels are interactively truncated and the boundaries are extruded in order to minimize the effects of boundary conditions in the region of the aneurysm.

Grid Generation: The anatomical model is then used as a support surface to generate a finite element grid using an advancing front method that first re-triangulates the surface and then marches into the domain generating tetrahedral elements [26]–[28]. Surface features such as ridges and corner points are automatically detected and preserved in the finite element grid. This approach does not require an analytical representation of the surface defining the computational domain, which is often a difficult step required by most commercial grid generation packages. The element size distribution appropriate for CFD calculations is obtained from source functions, automatically generated adaptive background grids [25].

B. Modeling Blood Flow

Governing Equations: Blood flow is mathematically modeled by the unsteady Navier–Stokes equations for an incompressible fluid [10], [34]

$$\nabla \cdot \mathbf{v} = 0 \tag{1}$$

$$\rho\left(\frac{\partial \mathbf{v}}{\partial t} + \mathbf{v}\cdot\nabla\mathbf{v}\right) = -\nabla p + \nabla\cdot\boldsymbol{\tau} + \mathbf{f} \tag{2}$$

where ρ is the density, $\mathbf{v}$ is the velocity field, p is the pressure, and $\boldsymbol{\tau}$ is the deviatoric stress tensor. Although the stress/strain-rate relationship is in general a tensor relation, it is usually expressed as an algebraic equation of the form

$$\tau = \mu\dot{\gamma} \tag{3}$$

where μ is the viscosity, and the strain-rate is defined as the second invariant of the strain-rate tensor, which for incompressible fluids is

$$\dot{\gamma} = 2\sqrt{\epsilon_{ij}\epsilon_{ij}} \tag{4}$$

and

$$\epsilon_{ij} = \frac{1}{2}\left(\frac{\partial v_i}{\partial x_j} + \frac{\partial v_j}{\partial x_i}\right). \tag{5}$$

In order to close the system of equations, a constitutive law must be provided to compute the local viscosity of the fluid. The simplest rheological model is a Newtonian fluid, which assumes a constant viscosity: $\mu = \mu_0$. Typical values used for blood are $\rho = 1.105\ \mathrm{g/cm^3}$ and $\mu = 0.04$ Poise. However, blood can be thought of as a suspension of particles (red blood cells) in an aqueous medium (plasma). Thus, it is neither homogeneous nor Newtonian. The rheological properties of blood are mainly dependent on the hematocrit, or the volume fraction of red blood cells in the blood. One of the most commonly used non-Newtonian fluid models for blood is the model of Casson [10], which assumes a stress/strain-rate relation of the form

$$\sqrt{\tau} = \sqrt{\tau_0} + \sqrt{\mu_0}\sqrt{\dot{\gamma}} \tag{6}$$

where τ_0 is the yield stress and μ_0 the Newtonian viscosity. The existence of a yield stress implies that blood requires a finite stress before it begins to flow, a fact that has been observed experimentally. The apparent viscosity of the Casson model can be written as

$$\mu = \left(\sqrt{\frac{\tau_0}{\dot{\gamma}}} + \sqrt{\mu_0}\right)^2. \tag{7}$$

Since this expression diverges as the strain-rate becomes zero, it is typically modified in the following way:

$$\mu = \left[\sqrt{\tau_0\left(\frac{1 - e^{-m\dot{\gamma}}}{\dot{\gamma}}\right)} + \sqrt{\mu_0}\right]^2 \tag{8}$$

where the parameter m controls the maximum viscosity obtained when $\dot{\gamma}$ tends to zero. Typical values used for blood are $\tau_0 = 0.04\ \mathrm{dyne/cm^2}$, $\mu_0 = 0.04\ \mathrm{dynes/cm}$, and $m = 100$.

Boundary Conditions: Physiologic boundary conditions are derived from phase-contrast magnetic resonance (MR) images of the main branches of the circle of Willis, of a normal volunteer [1], [17]. Time-dependent flow rates are obtained by integration of the measured velocity profile over the vessel cross section. The region of integration is either manually drawn on cross-sectional views or via threshold segmentation of the magnitude images. The curve is decomposed into Fourier modes

$$Q(t) = \sum_{n=0}^{N} Q_n e^{in\omega t} \tag{9}$$

where N is the number of modes, ω is the angular frequency obtained from the period of the cardiac cycle. The velocity profile is computed from the Womersley solution

$$v(r,t) = \frac{2Q_0}{\pi a^2}\left[1 - \left(\frac{r}{a}\right)^2\right] + \sum_{n=1}^{N}\frac{Q_n}{\pi a^2}\left[\frac{1 - \frac{J_0\left(\frac{\beta_n r}{a}\right)}{J_0(\beta_n)}}{1 - \frac{2J_1(\beta_n)}{\beta_n J_0(\beta_n)}}\right] e^{in\omega t} \tag{10}$$

where

$$\beta_n = i^{\frac{3}{2}}\alpha_n = i^{\frac{3}{2}} a\sqrt{\frac{n\omega}{\nu}}. \tag{11}$$

This profile is mapped to the inflow boundary using an algorithm that maps the surface mesh of the boundary to a circle [17].

Since flow rates are not available for all the branches included in the models, traction free boundary conditions are applied in all the outflow boundaries. This approach basically assumes that the flow divisions among the arterial branches is determined by the geometry of the anatomical model. However, it is known that the flow divisions are actually determined by the impedance of the distal arterial tree. The importance of prescribing the appropriate flow rates and flow divisions are studied in the following sections.

Vessel wall compliance is an important effect that may alter the local hemodynamics. Fluid-solid interaction algorithms have been applied to the study of these effects on the flow patterns [3]. However, the main problem remains the proper characterization of the arterial wall, i.e., the values of local material properties such as modulus of elasticity, wall thickness, etc. In addition, coupled fluid-solid models require the specification of proper pressure boundary conditions, i.e., the pressure waveform that drives the motion of the arterial wall, which is difficult to measure noninvasively [42]. For these reasons, the vessel walls are usually assumed rigid. The importance of this approximation remains to be studied. No-slip boundary conditions are applied at the vessel walls, i.e., the fluid velocity is equal to the velocity of the wall, which under the assumption of rigid vessel walls becomes $\mathbf{v} = 0$.

Numerical Solution: Over the years, several numerical schemes have been used to solve the incompressible Navier–Stokes Equations (2), (1) [4], [29], [30]. What sets incompressible flow solvers apart from compressible flow solvers is the fact that the pressure is not obtained from an equation of state but from the divergence constraint. In other words, the pressure establishes itself instantaneously and must, therefore, be integrated implicitly [35]. The equation for the pressure can be found by taking the divergence of the momentum (2)

$$\nabla^2 p = -\nabla\cdot(\mathbf{v}\cdot\nabla\mathbf{v}). \tag{12}$$

The hyperbolic character of the advection operator and the elliptic character of the pressure-Poisson equation have led to a number of so-called projection schemes. Our methodology is based on this approach and will be described in detail below. The timestep for explicit time integration schemes is restricted by stability constraints. The result is that for typical hemodynamics simulations several tens or hundreds of thousands of timesteps are required per cardiac cycle. The alternative is to

use fully implicit time integration schemes. The simplest such schemes can be written in the following form [31], [36]:

$$\frac{\mathbf{v}^{\theta}-\mathbf{v}^{n}}{\theta\Delta t}+\mathbf{v}^{\theta}\cdot\nabla\mathbf{v}^{\theta}+\nabla p^{\theta}=\nabla\mu\cdot\nabla\mathbf{v}^{\theta} \tag{13}$$

$$\nabla\cdot\mathbf{v}^{\theta}=0. \tag{14}$$

When $\theta=1$ the first order backward Euler scheme is recovered, while for $\theta=0.5$ the second order Cranck–Nicholson scheme is obtained. A fully implicit finite element formulation that yields stable solutions for arbitrary timesteps can be written as [31]

$$\begin{aligned}&\frac{1}{\Delta t}\left[(\mathbf{v}^{n+1,i},\mathbf{w})-(\mathbf{v}^{n},\mathbf{w})\right]+(\mathbf{v}^{n+\theta,i-1}\cdot\nabla\mathbf{v}^{n+\theta,i},\mathbf{w})\\&\quad+(\nu\nabla\mathbf{v}^{n+\theta,i},\nabla\mathbf{w})-(p^{n+1,i-1},\nabla\cdot\mathbf{w})\\&\quad+\left(\tau[\mathbf{v}^{n+\theta,i-1}\cdot\nabla\mathbf{v}^{n+\theta,i}-\alpha\boldsymbol{\Pi}^{n+\theta,i-1}],\mathbf{v}^{n+\theta,i-1}\cdot\nabla\mathbf{w}\right)\\&\qquad=(\boldsymbol{\sigma}^{n+\theta,i-1}\cdot\mathbf{n},\mathbf{w})_{\Gamma}+(\mathbf{f}^{n+\theta},\mathbf{w})\end{aligned} \tag{15}$$

$$\begin{aligned}&\Delta t(\nabla p^{n+1,i}-\nabla p^{n+1,i-1},\nabla q)\\&\quad+\left(\tau[\nabla p^{n+1,i}-\alpha\boldsymbol{\xi}^{n+1,i-1}],\nabla q\right)\\&\qquad=-(\nabla\cdot\mathbf{v}^{n+1,i},q)\end{aligned} \tag{16}$$

where i is the subiteration level, $\mathbf{w}$ and q are the finite element test functions, $\boldsymbol{\sigma}$ the deviatoric stress tensor, (a,b) denotes the L^2 inner product taken over the computational domain Ω, Γ is the boundary of the domain, and $\mathbf{n}$ its outer normal. The local critical timestep or stabilization parameter τ is computed from the element Courant–Friedrich–Levy (CFL) condition

$$\tau=\frac{h^2}{2|\mathbf{v}|h+4\nu} \tag{17}$$

where h is the element size. The projected terms $\boldsymbol{\Pi}$ and ξ defined as

$$(\boldsymbol{\Pi}^{n+\theta,i},\mathbf{w})=(\mathbf{v}^{n+\theta,i}\cdot\nabla\mathbf{v}^{n+\theta,i},\mathbf{w}) \tag{18}$$

$$(\boldsymbol{\xi}^{n+1,i},\mathbf{w})=(\nabla p^{n+1,i},\mathbf{w}) \tag{19}$$

are treated explicitly using a lumped approximation of the mass matrix. The discretized momentum (15) is solved using a generalized minimal residual (GMRES) algorithm, while the pressure (16) is solved using an incomplete lower-upper (ILU) preconditioned conjugate gradient solver [46]. The algorithm is iterated to convergence in each timestep. Usually the residuals are required to converge three orders of magnitude in each timestep. This algorithm with a value of $\theta=1$ has demonstrated to be very robust, and, therefore, we used this value in our simulations.

C. Hemodynamic Characterization

In order to study possible associations between aneurysm rupture and hemodynamics, approximately 60 aneurysms have been classified into different categories according to different hemodynamic characteristics [16]. Briefly, the aneurysm hemodynamics was characterized according to the following criteria.

- The complexity of flow pattern (FP) was divided into four categories: 1) stable vector of inflow jet with a single associated vortex; 2) stable vector of inflow jet with multiple associated vortices but no change in the number of vortices during the cardiac cycle; 3) changing vector of inflow jet with creation of a single vortex; and 4) changing vector of the inflow jet with creation or destruction of multiple vortices.
- *Impingement region (IR):* the region where the flow impinges against the aneurysm wall was identified as neck, body, dome, lobulation or changing. These regions are qualitatively defined as schematically indicated in Fig. 1.
- The size of the flow impingement region (IS) was classified as small or large with respect to the area of the aneurysm sac.
- *Mean wall shear stress (WSS):* the region where the WSS is elevated with respect to the parent vessel was identified as uniform, neck, body, dome, or lobulation (see Fig. 1).

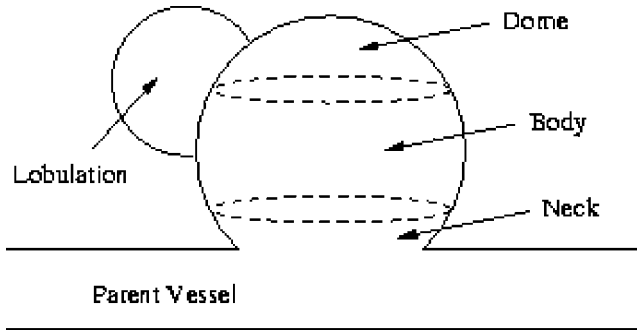

Fig. 1. Regions of an aneurysm.

TABLE I
THE LOCATIONS OF THE ANEURYSMS AND THE ARTERIES WHERE THE INFLOW WAVEFORMS WERE MEASURED

Model	Location	Side	Inflow	IR	IS	WSS
#1	ICA paraclinoid	right	ICA	body	large	body
#2	SCA	right	Basilar	neck	small	neck
#3	ICA PcomA	right	ICA	body	small	body
#4	ICA	right	ICA	dome	small	neck

ICA: internal carotid artery; SCA: superior cerebellar artery; PcomA: posterior communicating artery.

D. Sensitivity Analysis

A study of the sensitivity of the hemodynamic classification described in the previous section with respect to different modeling parameters and assumptions was carried out. Since variables such as time-dependent flow rates and flow divisions had to be prescribed from measurements performed on a normal volunteer due to a lack of personalized *in vivo* measurements, this sensitivity analysis is useful to assess whether changes in such variables would change the hemodynamic classification of a given aneurysm.

Four aneurysms were selected from the sample of 60, one of each FP category. In what follows, these models are denoted #1 for the aneurysm in FP category 1; #2 for the aneurysm in FP category 2; and so on. The base models were run using a Newtonian viscosity model under pulsatile flow conditions derived from PC-MR images of a normal volunteer in the corresponding feeding artery, and traction-free boundary conditions in all the outflow boundaries. Table I shows the classification of these aneurysms with respect to the IR, IS, and WSS variables defined in the previous section.

For the sensitivity analysis, the following parameters were changed and new CFD simulations were performed:

- *Mean Flow:* The total flow was increased and decreased by 25% with respect to the base value.
- *Flow Division:* For aneurysms #2 and #4, the flow division among the different arterial branches was varied. Since aneurysm #2 has four outflow vessels, eight different flow conditions were generated by raising and lowering the mean flow by 25% in each outflow branch independently keeping the inflow and the flow divisions among the other branches constant. Aneurysm #4 has two outflow vessels and one of these bifurcates immediately distal of the aneurysm. Thus, in this case, four flow conditions were generated: raising and lowering the mean flow by 25% in the nonbifurcating branch while keeping the inflow and the flow division between the other vessels constant, and by changing the flow division between the branches of the bifurcated vessel keeping the inflow and the flow in the un-bifurcated branch constant.
- *Small Vessels:* The small branches present in model #1 were closed, i.e., a $\mathbf{v} = 0$ boundary condition was prescribed in the outflow boundary of these branches.
- *Mesh Size:* Three grids with different number of elements were created for aneurysm #1. A small grid with a maximum element size of 0.4 mm contained 0.51×10^6 elements. A medium grid with a maximum element size of 0.2 mm contained 1.25×10^6 elements. And a large mesh with a maximum element size of 0.1 mm contained 4.61×10^6 elements. The first two meshes (small and medium) were generated using adaptive background grids that automatically increased the mesh resolution in regions of high vessel surface curvature. For the large mesh, a uniform element size distribution was prescribed.
- *Non-Newtonian Viscosity:* The fluid viscosity was allowed to change according to the non-Newtonian model of Casson.
- *Reconstruction:* Two extra modelers were asked to construct new anatomical models of each aneurysm from scratch.

A total of 39 CFD simulations were carried out and visualizations of the flow pattern for each case were produced. The new flow patterns were compared with the base case in order to determine if these variations in the model parameters actually changed the hemodynamic classification of the aneurysms.

III. Results

The four selected aneurysm models are shown in Fig. 2. Each row shows, from left to right, a volume rendering of the 3DRA images, the reconstructed model, the plane used to visualize the intra-aneurysmal flow pattern, and the input flow waveform with lines indicating the time frames of the subsequent visualizations. Note that the inflow curves for aneurysms #1, #3, and #4 correspond to flow rates measured in the ICA while the inflow curve for aneurysm #2 was taken from the measurement in the basilar artery. The simulations were run for two cardiac cycles using 100 timesteps per cycle, and all the visualizations were produced from the results of the second period.

Visualizations of the inflow region of each aneurysm under the base flow conditions at different instants during the cardiac cycle are presented in Fig. 3. Based on these visualizations, a plane was defined for each aneurysm (see Fig. 2) on which the major flow structures could be visualized and on which most of the changes were expected to ocurr. Then, for the sensitivity analysis, the intra-aneurysmal flow patterns were then only visualized on these planes as instantaneous velocity contours.

Visualizations of the flow pattern of aneurysm #1 under different conditions are shown in Fig. 4. Each column of this

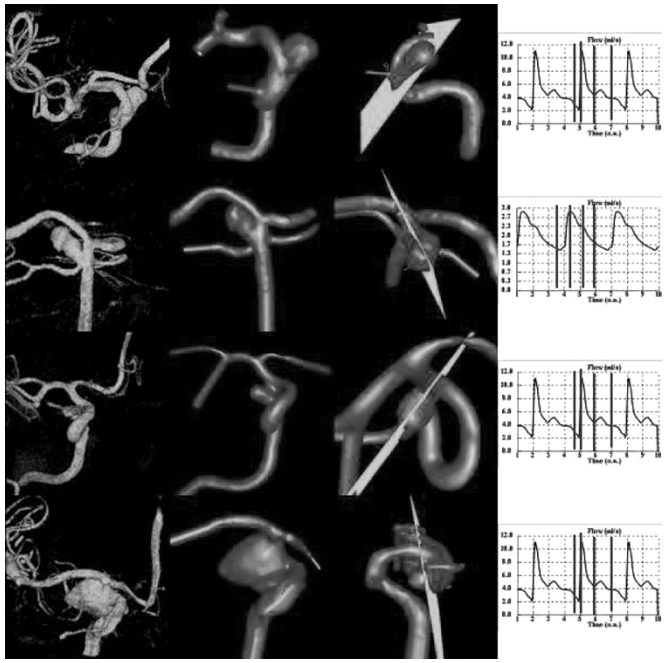

Fig. 2. Four aneurysm models reconstructed from 3DRA images. From left to right: volume rendering of the 3DRA images, reconstructed models, planes used to visualize the intra-aneurysmal flow patterns, input flow waveforms and time frames used in the visualizations.

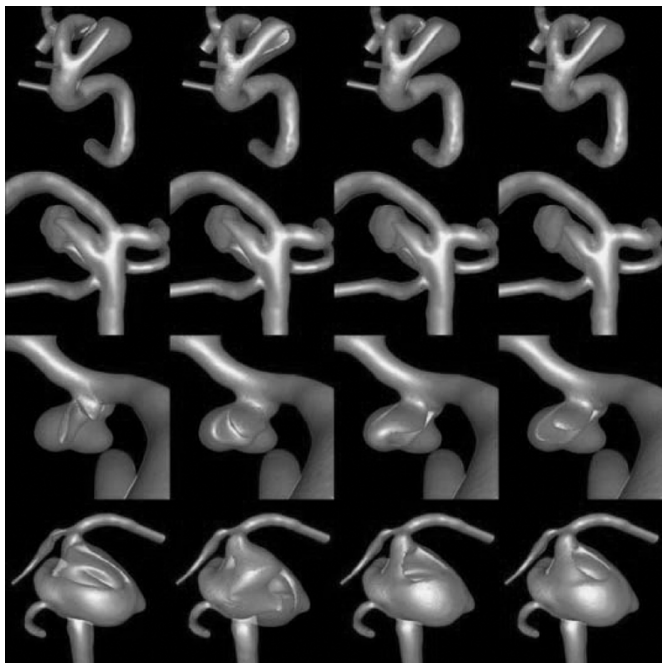

Fig. 3. Velocity isosurfaces at different instants of time during the cardiac cycle for each aneurysm under the base flow conditions. The iso-velocity values used are 15 cm/s, 5 cm/s, 10 cm/s, and 10 cm/s for aneurysms #1, #2, #3, and #4, respectively.

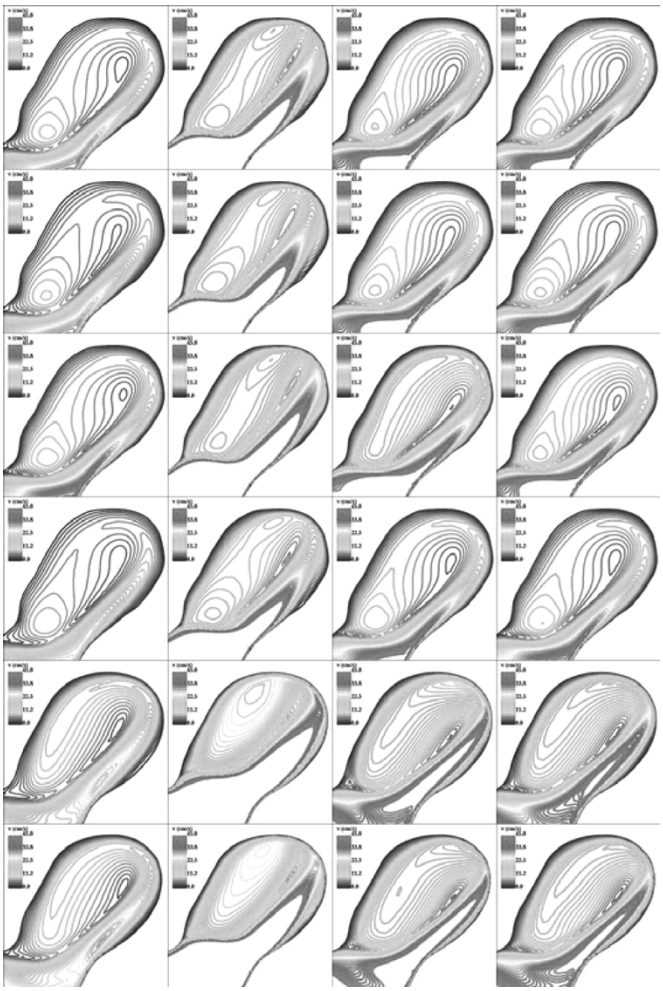

Fig. 4. Velocity contours on planar cut through aneurysm #1 at four instants during the cardiac cycle. From top to bottom: base model, Casson model, increased flow model, decreased flow model, model constructed by modeler #2, model created by modeler #3. Forty-five contours are plotted between 0 and 45 cm/s.

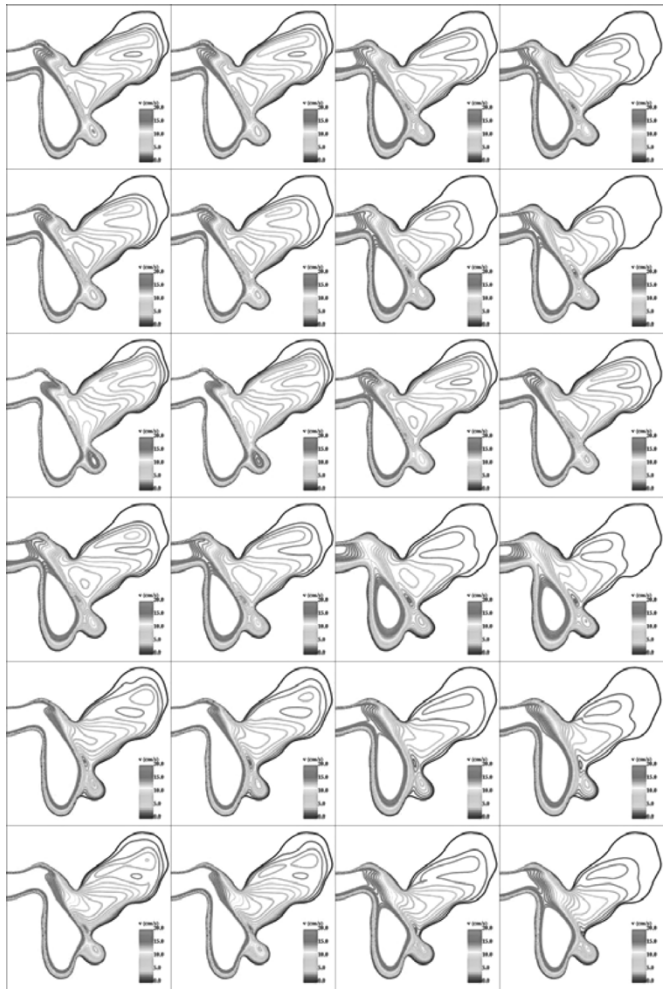

Fig. 5. Velocity contours on planar cut through aneurysm #2 at four instants during the cardiac cycle. From top to bottom: base model, Casson model, increased flow model, decreased flow model, model constructed by modeler #2, model created by modeler #3. Twenty contours are plotted between 0 and 20 cm/s.

figure corresponds to the instants of time indicated in Fig. 2. The rows correspond to: 1) the base model; 2) the Casson model; 3) increased mean flow model; 4) decreased mean flow model; 5) model constructed by modeler #2; and 6) model constructed by modeler #3.

Similar visualizations of the flow patterns computed for aneurysm #2, #3, and #4 are shown in Figs. 5, 6, and 7, respectively.

The flow patterns obtained for aneurysm #1 with the small branches closed are shown in Fig. 8 (top row). This figure also shows the results obtained using the coarse grid (second row), the medium size grid (third row), and the fine grid (bottom row).

Visualizations of the flow patterns obtained imposing different flow divisions for aneurysm #2 and #4 are shown in Figs. 9 and 10, and 11, respectively.

Finally, the mean wall shear stress distributions obtained under different conditions are shown in Fig. 12. The rows of this figure correspond to each of the four aneurysm models. The columns, from left to right, correspond to: 1) the base model; 2) the Casson model; 3) the increased flow model; and 4) the decreased flow model.

Effects of Flow Rate: Although the location and shape of the major vortex structures of the intra-aneurysmal flow patterns were slightly different for different flow rates, the classification of the aneurysms with respect to the complexity and stability of their FP remained unchanged (see rows 1, 3, and 4 of Figs. 4–7).

For aneurysms #1 and #2 mainly the magnitude of the velocity or the vortex intensity were affected by the flow rate but not the overall flow features. The largest differences in the intra-aneurysmal flow patterns were observed in aneurysms #3 and #4. However, these aneurysms would still be assigned to FP categories 3 and 4, respectively.

The location of elevated mean WSS of these aneurysms coincide with the region where the inflow jet impinges against the aneurysm wall. Although the size of the flow impingement region (IS) changed slightly for different flow rates, the location of the impingement region (IR) and of elevated WSS remain unaffected (see Fig. 12). Again, these visualizations show that the aneurysm classification based on the location and size of the flow impingement region and of elevated WSS with respect to the WSS in the parent vessel did not change when varying the mean inflow rate.

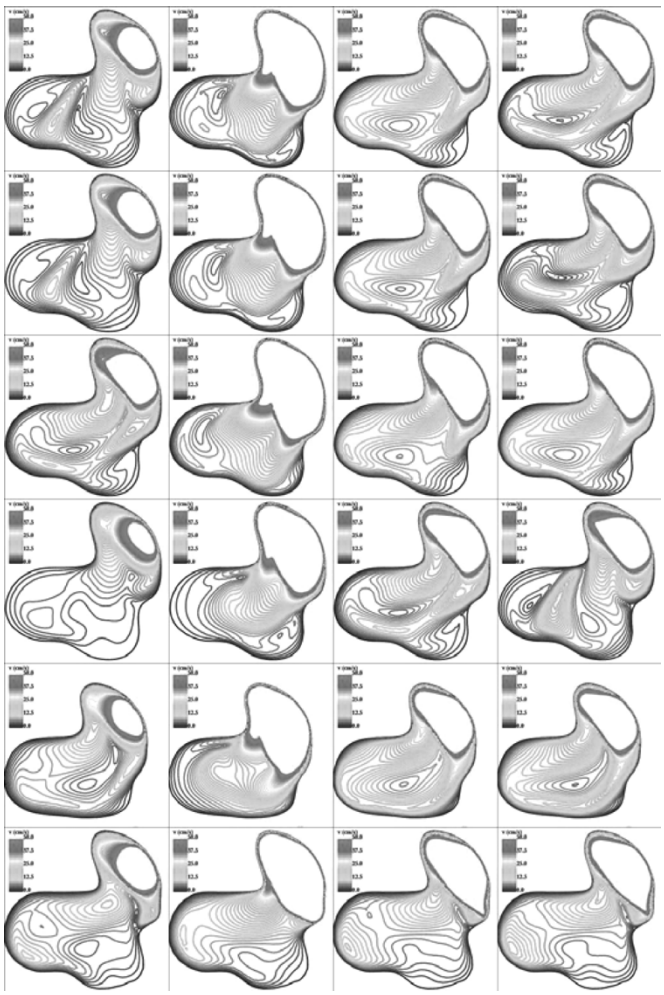

Fig. 6. Velocity contours on planar cut through aneurysm #3 at four instants during the cardiac cycle. From top to bottom: base model, Casson model, increased flow model, decreased flow model, model constructed by modeler #2, model created by modeler #3. Fifty contours are plotted between 0 and 50 cm/s.

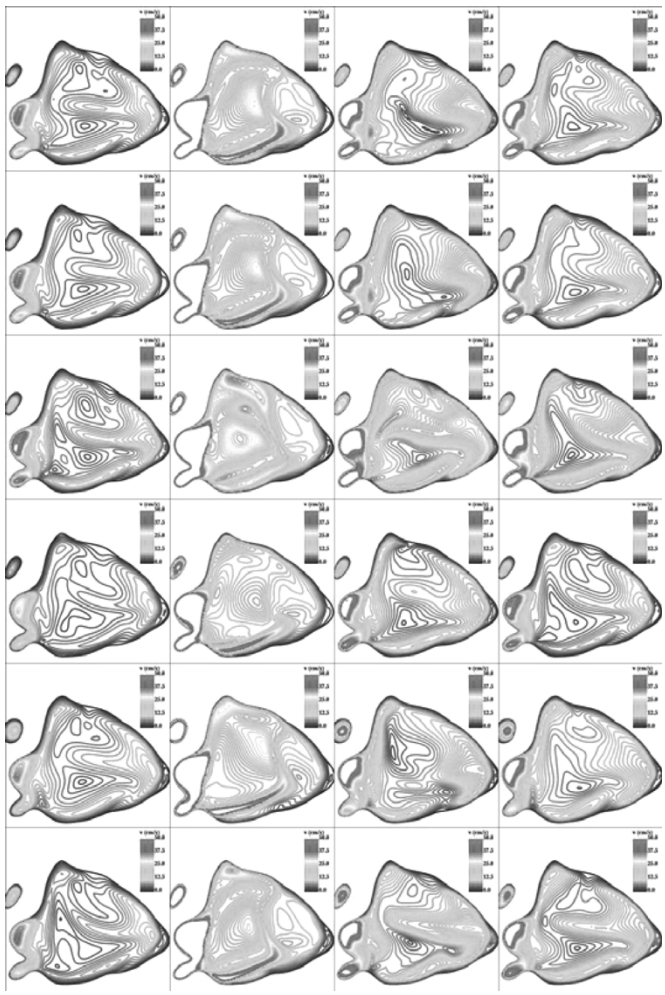

Fig. 7. Velocity contours on planar cut through aneurysm #4 at four instants during the cardiac cycle. From top to bottom: base model, Casson model, increased flow model, decreased flow model, model constructed by modeler #2, model created by modeler #3. Fifty contours are plotted between 0 and 50 cm/s.

Effects of Flow Division: Changing the flow division between the different branches of the models #2 and #4 did not alter the main characteristics of the intra-aneurysmal flow patterns (see Figs. 9, 10, and 11). Although some small scale details are different, especially for aneurysm #4, the flow patterns did not change in character with respect to our categorization.

Effects of Small Branches: No substantial differences were found between the flow patterns of the base model of aneurysm #1 (row 1 of Fig. 4) and the same model with the outflow boundaries of the small branches closed (row 1 of Fig. 8). This implies that small vessels branching off the parent artery are relatively unimportant with respect to the intra-aneurysmal flow pattern. However, vessel branches located on the aneurysm itself or its neck may be more important.

Effects of Mesh Size: The overall characteristics of the flow patterns of aneurysm #1 computed on three grids with different number of elements were quite similar. Although there are some small differences, the main flow features did not change significantly, even from the medium to the small grid. This indicates that, at least in some cases, the important flow features may be captured even with grids that contain a small number of elements.

Effects of Viscosity Model: The use of non-Newtonian viscosity models such as the Casson model tend to produce smaller velocity gradients than the Newtonian model. This is due to an increase of the local non-Newtonian viscosity in regions of low flow and low strain-rate. The overall flow pattern characteristics and distribution of mean WSS were relatively unaffected by the use of a non-Newtonian viscosity (see rows 1 and 2 of Figs. 4–7; and columns 1 and 2 of Fig. 12). The largest differences between the base Newtonian model and the Casson model were observed for aneurysm #2 which correspond to the aneurysm located in the basilar artery where the flow rate is relatively small and then non-Newtonian effects become more important. Even though, some changes were observed in the main flow characteristics and the distribution of mean WSS, the classification of the aneurysm with respect to FP, IR, IS, and WSS was not affected by the choice of viscosity model.

Effects of Reconstruction: The flow patterns computed using each of the models reconstructed by the three modelers were in good agreement. Again, only minor differences that did not change significantly the flow structure were observed, with the exception of the model constructed by modeler #2 of aneurysm #3 (row 5 of Fig. 6). In this case, a small difference in the geometry of the anatomical models constructed by different modelers resulted in a substantial difference in the intra-aneurysmal

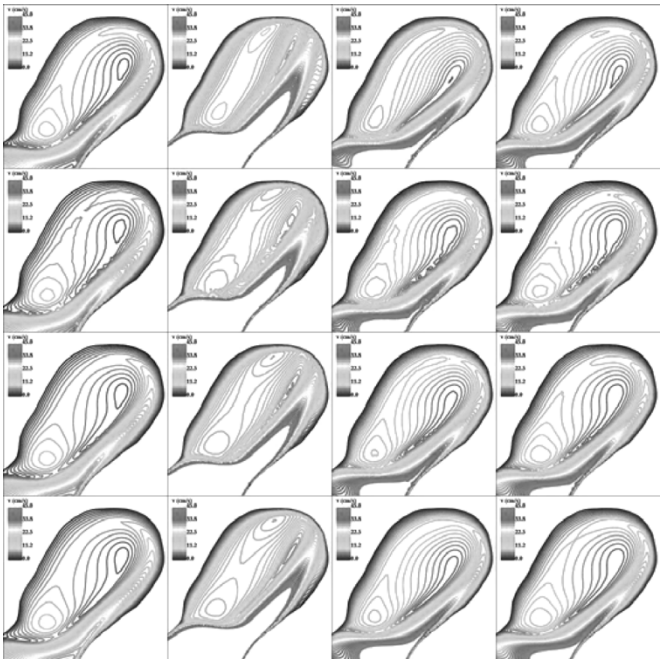

Fig. 8. Effects of small branches and grid resolution on flow pattern of aneurysm #1. From top to bottom: model with small branches closed, coarse grid, medium size grid, fine grid. Forty-five velocity contours are plotted between 0 and 45 cm/s.

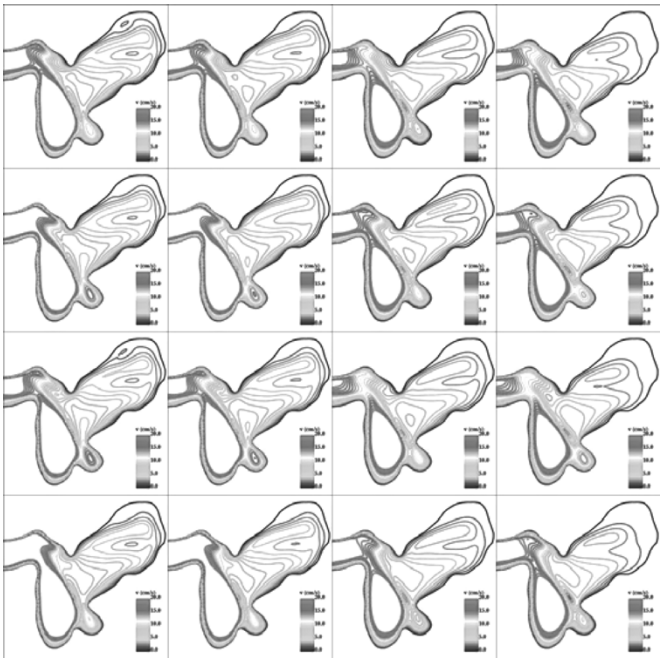

Fig. 9. Effects of flow division on flow pattern of aneurysm #2 obtained by increasing and lowering the mean flow by 25% through each arterial branch independently. Twenty velocity contours are plotted between 0 and 20 cm/s.

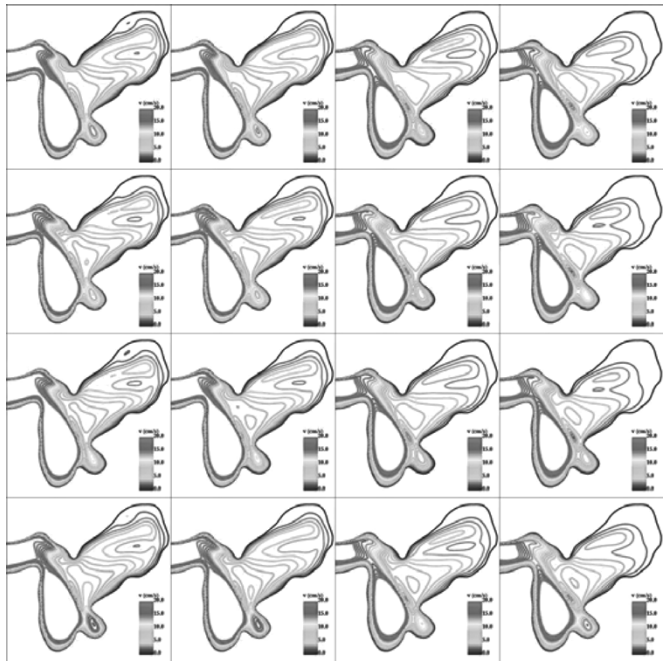

Fig. 10. Effects of flow division on flow pattern of aneurysm #2 obtained by increasing and lowering the mean flow by 25% through each arterial branch independently. Twenty velocity contours are plotted between 0 and 20 cm/s.

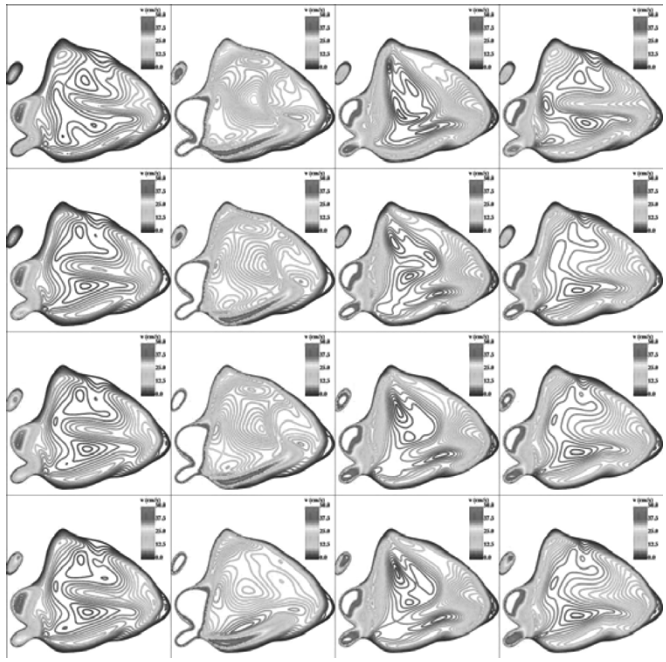

Fig. 11. Effects of flow division on flow pattern of aneurysm #4 obtained by increasing and lowering the mean flow by 25% through each arterial branch independently. Fifty velocity contours are plotted between 0 and 50 cm/s.

flow structures. This small geometrical difference comes from the fact that the parent vessel (the internal carotid artery) passes very close to the dome of the aneurysm. As a consequence, the segmentation algorithm failed to separate the sac from the vessel due to the limited resolution of the anatomical image. Therefore, the surface had to be manually edited in order to correct the topology of the model, i.e., separate the sac from the vessel. This manual editing is what caused the difference in the geometry of the models. A superposition of the models constructed by modeler #1 and modeler #2 is shown in Fig. 13.

IV. Discussion

The pipeline described for constructing realistic patient-specific models of the hemodynamics in cerebral aneurysms is efficient and is able to handle many different aneurysms types, sizes and shapes.

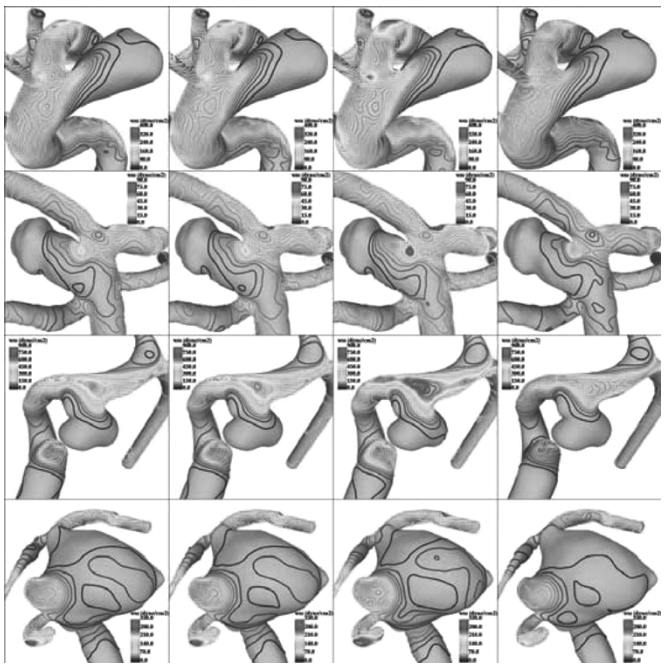

Fig. 12. Visualizations of mean wall shear stress distributions for the four aneurysm models. From left to right: base model, Casson model, increased mean flow model, decreased mean flow model. Contours are plotted in intervals of 10 $\mathrm{dyne/cm^2}$ between 0 and 400 $\mathrm{dyne/cm^2}$, 90 $\mathrm{dyne/cm^2}$, 900 $\mathrm{dyne/cm^2}$, and 350 $\mathrm{dyne/cm^2}$ for aneurysms #1, #2, #3, and #4, respectively.

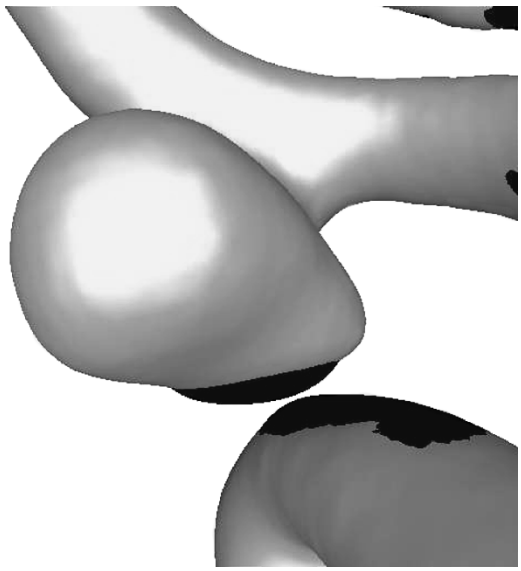

Fig. 13. Superposition of the models constructed by two different modelers showing a small difference in the geometries that caused significant changes in the flow structure. This difference comes from the manual editing performed to separate the aneurysm sac from the parent vessel.

All the models presented in this paper were constructed from 3DRA images because they are readily available from routine clinical examinations. However, the methodology is not restricted to 3DRA images, in fact several models of cerebral aneurysms have been constructed from computed tomography angiography (CTA) images [13], [14] and magnetic resonance angiography (MRA) images [12]. This is an important property since these modalities could be used to follow up unruptured aneurysms that are left untreated or to construct aneurysms that were incidentally discovered. Different image modalities used to depict the vessels and the aneurysms have different levels of difficulties associated to the reconstruction process. Both CTA and MRA images have much less contrast between the blood vessels and the surrounding tissue than 3DRA images that are produced during intraarterial injection of contrast. In addition, bone structures are usually bright in CTA images making the reconstruction of aneurysms that are close to the bone more problematic. Further studies with images from different modalities are needed to test and improve the methodology.

The image-based methodology has been extensively validated with data from similar applications. In particular, numerical results have been found in good agreement with data measured in idealized *in vitro* models of stenosed carotid [3] and renal arteries [33], as well as *in vivo* data from normal [3] and stenosed carotid arteries [11]. However, there is still need for quantitative validation of the numerical models against experimental and *in vivo* data from aneurysmal vascular structures. This is an open problem that has not been fully addressed to date. A major portion of our efforts are currently devoted to this problem and to demonstrate the clinical utility of the information derived from these computational models.

The construction of a model from anatomical images is a semi-automatic process only taking a couple of hours of labor. The grid generation process is completely automated, and the flow solution can be obtained in about 14 h/cardiac cycle on a Pentium4 processor PC with 2 GB of RAM for a grid of approximately 2 million elements. The postprocessing and visualization process is also semi automatic. Once the modeler specifies the desired flow visualizations they are automatically produced using a visualization software with a scripting capability [18]. The complete process of model construction, meshing, CFD calculation and visualization can be completed in a day for the two cardiac cycle visualizations used for this study. However, the methodology still needs to be adapted to be used routinely in clinical environments by nonexpert users. In other words, before these techniques can be routinely used for clinical purposes, it is necessary to clearly identify which hemodynamic parameters provide the most useful information to clinically evaluate the risk of rupture (e.g., location and size of the flow impingement region or flow complexity) and to develop methods to objectively extract these quantities from the numerical solutions. Secondly, the entire modeling process needs further automation to minimize the required user intervention which currently requires high level of expertise. Finally, the total computation time needs to be reduced. This can be achieved by further optimization of several of the grid generation and flow solution algorithms.

One of the limitations of most previous approaches is that the modeling pipeline from medical images to flow simulations is not optimized and many stages require substantial user intervention and editing. In fact, most recent studies of CFD in brain aneurysms have been confined to simulation in only a very few cases [6], [7], [22], [41]. Additionally, many of these methods would be unable to handle the problem of grid generation when confronted with realistic complex geometries of aneurysms, its connected vessels and possibly endovascular devices. However, the methodology presented in this paper is efficient and allows the modeling of a large number of aneurysms in a timely manner adequate for clinical studies. In fact, a database of approximately 60 aneurysm model has been constructed over the past six months using this approach [13]–[16].

As with many CFD modeling approaches, our methodology also has some practical and theoretical limitations in its attempt to recreate the real world conditions of a cerebral aneurysm. This model assumes rigid vessel walls, the aneurysm is studied in isolation from the surrounding vasculature of the cerebral circulation, and rotational 3-D cerebral angiography obtained from routine clinical cases may not be complete enough to model all aneurysm types (i.e., aneurysms receiving major inflows from two different cerebral arteries may not be completely visualized when only one 3DRA is done).

Rigid walls of the model were chosen due to a lack of information regarding arterial wall properties such as elasticity and thickness, and the intraarterial pressure waveforms needed to prescribe physiologically correct boundary conditions for fluid-structure interaction algorithms. Intraarterial pressure measurements in cerebral aneurysm patients are not a routine examination in clinical practice. Many of the techniques needed to make these measurements are costly or invasive. So, until it is shown that hemodynamic forces can be determined and will have a potential clinical impact on patient care, further study of patient-specific wall compliance effects will be difficult. Currently, the importance of wall compliance effects on the intra-aneurysmal flow patterns and distributions of hemodynamic forces on the aneurysmal wall remains to be studied.

Modeling aneurysms that have a major inflow from more than one cerebral artery represents a challenge to this CFD modeling approach. This typically occurs with 3DRA images of anterior communicating artery aneurysms or vertebrobasilar junction aneurysms because usually only the left or right arterial trees are imaged using an intraarterial injection of contrast material in either the left or right side. Therefore, the contralateral feeding arteries are not imaged and, thus, cannot be accurately modeled. This problem could be solved by a second injection in the contralateral internal carotid artery, but this may not always be clinically justified. Even if this second image is obtained, there are complications associated with the registration of the two images or models.

Despite these limitations, our sensitivity analysis suggests that the CFD methodology may still provide a reasonable approximation of the hemodynamics of *in vivo* conditions and may be useful for clinical studies of aneurysmal rupture.

Preliminary results from a pilot clinical study of cerebral aneurysm rupture [16] have shown interesting trends in the distribution of ruptured and unruptured aneurysms with respect to hemodynamic categories such as those described in Section II-C. For instance, it was found that unruptured aneurysms tend to have simple and stable flow pattern (FP category 1) and large regions of flow impingement (IR), while ruptured aneurysms tend to have more complex and unstable flow patterns and small impingement zones. Presumably, concentrating forces transferred from the inflow jet into a small area of impingement imply that there are associated larger values of wall shear stress and pressure confronted by the aneurysm wall and a higher likelihood of localized damage. Conversely, an equal amount of flow striking the wall at a larger zone would result in a lower and presumably safer forces. We speculate that an unstable flow pattern could be associated with aneurysm progression and rupture because of the potential for oscillating forces on the vessel wall or larger regions of elevated wall shear stress that may lead to structural destabilization and failure. Alternatively, a stable flow pattern of repetitive forces may be more amenable to the arterial compensatory mechanisms for mitigating the stress making these aneurysms safer. Although the aforementioned pilot study provides a very useful guide as to which hemodynamic variables may be important to assess the risk of rupture, it needs to be extended in order to achieve higher statistical significance and to better define the hemodynamic characterization system. This is part of our current research effort.

The results of the sensitivity analysis presented in this paper indicate that, at least for some aneurysms, the flow conditions are not of primary importance for characterizing the intra-aneurysmal hemodynamics. Only if accurate quantitative estimations of the hemodynamic forces on the aneurysmal wall are required, the measurement of the flow conditions (input flow rate and flow divisions among the branches) becomes necessary. Qualitatively little difference was seen for sizable variations of the input flow rate and flow divisions in the aneurysms studied.

Similar observations can be made regarding the non-Newtonian properties of blood. Newtonian models appear adequate for characterizing the intra-aneurysmal hemodynamics, but may not be appropriate for quantitative estimation of the hemodynamic forces on the aneurysm wall.

Taking into account small vessels branching off the parent vessel of the aneurysm has little effect on the intra-aneurysmal flow pattern. The most significant effect of these branches is in the mean wall shear stress in the region of the origin of such branches.

The results presented in this paper also indicate that the most important factor for determining the intra-aneurysmal flow pattern is the geometry of the aneurysm and the connected vessels. Due to the nonlinear character of the Navier–Stokes equations, relatively small changes in the geometry of the anatomical models can have significant effects on the flow characteristics. Any manual stage of the modeling pipeline can result in important geometric inaccuracies. Special care must be taken to prevent or minimize these errors until fully automatic and robust reconstruction methods become available.

V. Conclusion

An efficient image-based computational modeling pipeline has been described for the analysis of aneurysmal hemodynamics on a patient-specific basis.

A simple aneurysm classification system based on the most prominent intra-aneurysmal hemodynamic characteristics was created. Preliminary studies show potential associations between the flow categories and aneurysmal rupture.

Some understanding of the practical and theoretical limitations of the numerical models used for those studies can be gained by performing sensitivity analysis by adjusting a single variable over the expected physiologic range of conditions. The sensitivity analysis presented in this paper seem to indicate that the characterization of the intra-aneurysmal flows was not substantially altered when the mean inflow rate, the flow division, the viscosity model, or the mesh resolution were changed. In addition, it was seen that the models are most sensitive to variations in the vascular geometry.

Sensitivity analysis is a useful method of understanding the interaction of variables used for the CFD process but does not supplant the need for validation of the CFD models using *in vitro*, animal and *in vivo* data. Determining the accuracy of the computational models will be critical prior to any quantitative

study of hemodynamic forces. These flow related forces have the potential to be the input function for further CFD models incorporating the mechanical properties of the vessel walls for study of material failure rates.

In conclusion, with the proposed modeling pipeline clinical studies of cerebral aneurysms hemodynamics are feasible. In absence of flow information, sensitivity analyses similar to the one presented in this paper should be conducted in order to ensure a proper characterization of the intra-aneurysmal hemodynamics. Special attention should be paid to obtain accurate geometrical models since the flow patterns strongly depend on the shape of the aneurysm sac.

REFERENCES

[1] J. R. Cebral, M. A. Castro, R. Löhner, O. Soto, P. J. Yim, and N. Alperin, "Finite element modeling of the circle of willis from magnetic resonance data," *Proc. SPIE Med. Imag.*, vol. 5031, pp. 11–21, 2003.

[2] J. R. Cebral and R. Löhner, "From medical images to anatomically accurate finite element grids," *Int. J. Num. Meth. Eng.*, vol. 51, pp. 985–1008, 2001.

[3] J. R. Cebral, P. J. Yim, R. Löhner, O. Soto, and P. L. Choyke, "Blood flow modeling in carotid arteries using computational fluid dynamics and magnetic resonance imaging," *Acad. Radiol.*, vol. 9, pp. 1286–1299, 2002.

[4] F. Thomaset, *Implementation of Finite Element Methods for Navier–Stokes Equations*. Berlin, Germany: Springer-Verlag, 1981.

[5] A. F. Frangi, W. J. Niessen, K. L. Vincken, and M. A. Viergever, "Multiscale vessel enhancement filtering," in *Lecture Notes in Computer Science*. Berlin, Germany: Springer-Verlag, 1998, vol. 1496, Medical Image Computing and Computer-Assisted Interventions—MICCAI'98, pp. 130–137.

[6] T. Hassan, E. V. Timofeev, M. Ezura, T. Saito, A. Takahashi, K. Takayama, and T. Yoshimoto, "Hemodynamic analysis of an adult vein of galen aneurysm malformation by use of 3D image-based computational fluid dynamics," *AJNR Am. J.*, vol. 24, no. 6, pp. 1075–1082, 2003.

[7] T. Hassan, M. Ezura, E. V. Timofeev, T. Tominaga, T. Saito, A. Takahashi, K. Takayama, and T. Yoshimoto, "Computational simulation of therapeutic parent artery occlusion to treat giant vertebrobasilar aneurysm," *AJNR Am. J.*, vol. 25, no. 1, pp. 63–68, 2004.

[8] M. Hernandez, R. Barrena, G. Hernandez, G. Sapiro, and A. F. Frangi, "Pre-clinical evaluation of implicit deformable models for three-dimensional segmentation of brain aneurysms from CTA images," *Proc. SPIE Med. Imag.*, vol. 5032, pp. 1264–1274, 2003.

[9] J. Huang and J. M. van Gelder, "The probability of sudden death from rupture of intracranial aneurysms: a meta-analysis," *J. Neurosurg.*, vol. 51, no. 5, pp. 1101–1105, 2002.

[10] J. Mazumdar, *Biofluid Mechanics*. Singapore: World Scientific, 1992.

[11] J. R. Cebral, C. M. Putman, R. Pergolizzi, J. E. Burgess, and P. J. Yim, "Multi-modality image-based modelin of carotid artery hemodynamics," *Proc. SPIE Med. Imag.*, vol. 5369, pp. 529–538, 2004.

[12] J. R. Cebral, M. Castro, T. Satoh, and J. E. Burgess, "Evaluation of image-based cfd models of cerebral aneurysms using mri," presented at the *ISMRM Flow Motion Workshop*, Zurich, Switzerland, July 11–13, 2004.

[13] J. R. Cebral, M. Hernandez, and A. F. Frangi, "Computational analysis of blood flow dynamics in cerebral aneurysms from cta and 3D rotational angiography image data," presented at the *ICCB03*, Zaragoza, Spain, Sept. 24–26, 2003.

[14] J. R. Cebral, M. Hernandez, A. F. Frangi, C. M. Putman, R. Pergolizzi, and J. E. Burgess, "Subject-specific modeling of intracranial aneurysms," *Proc. SPIE Med. Imag.*, vol. 5369, pp. 319–327, 2004.

[15] J. R. Cebral, M. A. Castro, J. E. Burgess, and C. M. Putman, "Cerebral aneurysm hemodynamics modeling from 3D rotational angiography," presented at the *ISBI 2004*, Arlington, VA, Apr. 15–18, 2004.

[16] J. R. Cebral, M. A. Castro, J. E. Burgess, R. Pergolizzi, and C. M. Putman, "Characterization of cerebral aneurysm for assessing risk of rupture using patient-specific computational hemodynamics models," *AJNR Am. J. Neuroradiol.*, 2005, to be published.

[17] J. R. Cebral, M. A. Castro, O. Soto, R. Löhner, and N. Alperin, "Blood-flow models of the circle of willis from magnetic resonance data," *J. Eng. Math.*, vol. 47, pp. 369–386, 2003.

[18] J. R. Cebral and R. Löhner, "Interactive On-Line Visualization and Collaboration for Parallel Unstructured Multidisciplinary Applications," American Institute of Aeronautics and Astronautics, Reston, VA, Tech. Rep. AIAA-98-0077, 1998.

[19] J. W. Hop, G. J. Rinkel, A. Algra, and J. van Gijn, "Case-fatality rates and functional outcome after subarachnoid hemorrhage: a systematic review," *Stroke*, vol. 28, pp. 660–664, 1997.

[20] M. Kaminogo, M. Yonekura, and S. Shibata, "Incidence and outcome of multiple intracranial aneurysms in a defined population," *Stroke*, vol. 34, no. 1, pp. 16–21, 2003.

[21] K. N. T. Kayembe, M. Sasahara, and F. Hazama, "Cerebral aneurysms and variations of the circle of Willis," *Stroke*, vol. 15, pp. 846–850, 1984.

[22] L. D. Jou, C. M. Quick, W. L. Young, M. T. Lawton, R. Higashida, A. Martin, and D. Saloner, "Computational approach to quantifying hemodynamic forces in giant cerebral aneurysms," *AJNR Am. J. Neuroradiol.*, vol. 24, no. 9, pp. 1804–1810, 2004.

[23] F. H. Linn, G. J. Rinkel, A. Algra, and J. van Gijn, "Incidence of subarachnoid hemorrhage: role of region, year, and rate of computed tomography: a meta-analysis," *Stroke*, vol. 27, no. 4, pp. 625–629, 1996.

[24] T. M. Liou and S. N. Liou, "A review of *in vitro* studies of hemodynamic characteristics in terminal and lateral aneurysm models," *Proc. Nat. Sci. Council ROC(B)*, vol. 23, no. 4, pp. 133–148, 1999.

[25] R. Löhner, "Extensions and improvements of the advancing front grid generation technique," *Comm. Num. Meth. Eng.*, vol. 5, pp. 119–132, 1996.

[26] ——, "Regridding surface triangulations," *J. Comp. Phys.*, vol. 126, pp. 1–10, 1996.

[27] ——, "Automatic unstructured grid generators," *Finite Elements Anal. Design*, vol. 25, pp. 111–134, 1997.

[28] ——, "Renumbering strategies for unstructured grid solvers operating on shared memory, cached based parallel machines," *Comp. Meth. Appl. Mech. Eng.*, vol. 163, pp. 95–109, 1998.

[29] M. D. Gunsburger and R. Nicolaides, Eds., *Incompressible Computational Fluid Dynamics: Trends and Advances*. Cambridge, U.K.: Cambridge Unive. Press, 1993.

[30] M. M. Hafez, *Numerical Simulation of Incompressible Flows*. Singapore: World Scientific, 2003.

[31] O. Soto, R. Löhner, J. R. Cebral, and F. Camelli, "A stabilized edge-based implicit incompressible flow formulation," *Comput. Meth. Appl. Mech. Eng.*, vol. 193, pp. 2139–2154, 2004.

[32] P. J. Yim, B. C. Vasbinder, V. B. Ho, and P. L. Choyke, "Isosurfaces as deformable models for magnetic resonance angiography," *IEEE Trans. Med. Imag.*, vol. 4684, no. 7, pp. 1390–1397, Jul. 2003.

[33] P. J. Yim, J. R. Cebral, A. Weaver, R. J. Lutz, G. Boudewijn, C. Vasbinder, V. Ho, and P. L. Choyke, "Estimation of pressure gradients at renal artery stenoses," *MRM*, vol. 51, pp. 969–977, 2004.

[34] P. K. Kundu and I. M. Cohen, *Fluid Mechanics*. Amsterdam, The Netherlands: Elsevier, 2004.

[35] R. Löhner, *Applied CFD Techniques*. New York: Wiley, 2001.

[36] R. Löhner, C. Yang, J. R. Cebral, O. Soto, F. Camelli, and J. Waltz, "Improving the Speed and Accuracy of Projection-Type Incompressible Flow Solvers," American Institute of Aeronautics and Astronautics, Reston, VA, Tech. Rep. AIAA-03-3991-CP, 2003.

[37] T. W. Raaymakers, G. J. Rinkel, M. Limburg, and A. Algra, "Mortality and morbidity of surgery for unruptured intracranial aneurysms: a meta-analysis," *Stroke*, vol. 29, no. 8, pp. 1531–1538, 1998.

[38] R. W. Metcalfe, "The promise of computational fluid dynamics as a tool for delineating therapeutic options in the treatment of aneurysms," *AJNR Am. J. Neuroradiol.*, vol. 24, pp. 553–554, 2003.

[39] J. A. Sethian, *Level Set Methods and Fast Marching Methods: Evolving Interfases, in Computational Geometry, Fluid Mechanics, Computer Vision, and Materials Sciences*, ser. no. 3, Monographs on Applied and Computational Mathematics. Cambridge, U.K.: Cambridge Univ. Press, 1999.

[40] W. E. Stehbens, "Intracranial arterial aneurysms," in *Pathology of the Cerebral Blood Vessels*. St. Louis, MO: Mosby, 1972, pp. 351–470.

[41] D. A. Steinman, J. S. Milner, C. J. Norley, S. P. Lownie, and D. W. Holdworth, "Image-based bomputational simulation of flow dynamics in a giant intracranial aneurysm," *AJNR Am. J. Neuroradiol.*, vol. 24, no. 4, pp. 559–566, 2003.

[42] S. Z. Zhao, X. Y. Xu, A. D. Hughes, S. A. Thom, A. V. Stanton, B. Ariff, and Q. Long, "Blood flow and vessel mechanics in a physiologically realistic model of a human carotid arterial bifurcation," *J. Biomech.*, vol. 33, pp. 975–984, 2000.

[43] G. Taubin, "A signal processing approach to fair surface design," in *Proc. Computer Graphics*, 1995, pp. 351–358.

[44] F. Tomasello, D. D'Avella, F. M. Salpietro, and M. Longo, "Asymptomatic aneurysms. Literature metaanalysis and indications for treatment," *J. Neurosurg. Sci.*, vol. 42, no. 1, pp. 47–51, 1998.

[45] H. R. Winn, J. A. Jane, J. Taylor, D. Kaiser, and G. W. Britz, "Detection of asymptomatic incidental aneurysms: review of 4568 arteriograms," *J. Neurosurg.*, vol. 96, no. 1, pp. 43–49, 2002.

[46] Y. Saad, *Iterative Methods for Sparse Linear Systems*. Boston, MA: PWS Pub. Co., 1996.